3D Ultrasonic Wave Simulations for Structural Health Monitoring

Cara A.C. LECKEY [1], Corey A. MILLER[2], and Mark K. HINDERS[2]

[1]National Aeronautics and Space Administration, Langley Research Center, Hampton, VA, USA;
email: cara.ac.leckey@nasa.gov
[2]Department of Applied Science, College of William and Mary, Williamsburg, VA, USA

Abstract
Structural health monitoring (SHM) for the detection of damage in aerospace materials is an important area of research at NASA. Ultrasonic guided Lamb waves are a promising SHM damage detection technique since the waves can propagate long distances. For complicated flaw geometries experimental signals can be difficult to interpret. High performance computing can now handle full 3-dimensional (3D) simulations of elastic wave propagation in materials. We have developed and implemented parallel 3D elastodynamic finite integration technique (3D EFIT) code to investigate ultrasound scattering from flaws in materials. EFIT results have been compared to experimental data and the simulations provide unique insight into details of the wave behavior. This type of insight is useful for developing optimized experimental SHM techniques. 3D EFIT can also be expanded to model wave propagation and scattering in anisotropic composite materials.
Keywords: Structural health monitoring, simulation, Lamb waves

1 Introduction

Developing optimized flaw detection techniques for aerospace materials is an important area of research in the fields of nondestructive evaluation (NDE) and structural health monitoring (SHM). As more advanced materials, such as composites, are developed and utilized in the aerospace industry, efficient and accurate damage detection techniques will be necessary to ensure vehicle/component safety and functionality. A benefit of SHM on-board sensor techniques over traditional ground based NDE is the potential detection of in-flight material damaging events (which could be particularly critical for future long-duration spaceflight vehicles). Current techniques used for finding flaws in aerospace materials include visual inspection, shearography, acoustic emission, eddy current testing, ultrasonics, and other methods. A review of SHM techniques currently used to find damage in composite aircraft material can be found in a recent paper by Diamanti [1]. An advancement in current techniques will be necessary for the realization of economical, efficient, and accurate SHM systems for aerospace vehicles.

Guided Lamb waves are particularly ideal for detecting flaws in the plate and pipe-like structures that make up aerospace vehicles because the waves can propagate over long distances (tens of meters) and can be sensitive to some flaw types that are difficult to find using traditional ultrasound techniques [2, 3]. Additionally, the use of multiple Lamb wave modes could allow for flaw detection throughout the depth of a material since each mode has a different depth dependent displacement curve [4]. Active sensors such as embedded/attached piezoelectric wafers, interdigital transducers, and macrofiber composites may be ideal for generating and detecting Lamb waves in SHM applications, where light-weight (and potentially flexible) sensors are required [5–7]. Several review articles discuss various aspects of the use of Lamb waves in SHM [5, 8].

Lamb waves are created due to the stress-free boundaries of the plate-like material. A coupling of longitudinal and shear waves leads to the creation of any number of dispersive Lamb wave modes, which separate into antisymmetric and symmetric modes in an isotropic medium [4]. Although Lamb waves are described using the same elastodynamic equations as bulk waves, the presence of the plate boundaries leads to dispersion relations that must be solved numerically. The use of Lamb waves for nondestructive testing can be found in the literature as early as the 1950s [9], yet the complicated behavior of these dispersive waves has resulted in an extensive ongoing body of literature on guided wave based flaw detection. Techniques that excite multiple Lamb wave modes are much simpler than those required to create only one or two desired modes [8]. However, the generation of multiple Lamb wave modes leads to complicated wave behavior that can require sophisticated signal processing techniques to make sense of the data [10].

One way to provide insight into the complex behavior of Lamb wave interaction with flaws is to use numerical methods to simulate the Lamb wave propagation and scattering. The recent progress in computational power and availability allows us to run full 3-dimensional (3D) Lamb wave simulations using a computing cluster. In this paper we discuss the development, verification, and validation of an isotropic 3D simulation code that can be used to investigate Lamb wave behavior and interaction with material damage. One example of a longer term goal for these types of simulations would be to provide insight into optimal ultrasonic sensor configurations for a specific SHM application. We also discuss the extension of the simulation code to include anisotropic behavior for modeling Lamb waves in composites. In the following section we describe the specific numerical method, called finite integration technique (FIT), that we have used to implement 3D Lamb wave simulations.

2   Finite Integration Technique

FIT was developed by Weiland in 1977 for electrodynamics modeling, and was applied to elastodynamics by Fellinger in the early 1990s [11, 12]. Since that time, the elastodynamic finite integration technique (EFIT) has been used to explore elastic wave behavior in a variety of applications. Marklein's review paper gives a thorough overview of the history of FIT [13]. EFIT has been used over the last couple decades to investigate nondestructive evaluation applications such as scattering from flaws in plates, pipes, and bulk material [14, 15]. The technique has also been implemented to explore elastic wave propagation in anisotropic heterogeneous media for applications ranging from wave scattering from surface breaking cracks in steel welds to wave propagation in composites [16–18]. However, the majority of prior publications relating to EFIT have been limited to 2D simulations.

We chose FIT over other numerical techniques, such as finite difference and finite element method, for several reasons: 1) FIT naturally requires staggered spatial and temporal grids which leads to stability, 2) boundary conditions are easily incorporated into FIT, and 3) the mathematical analysis is straight-forward and leads to equations that are easy to implement in any programming language [13]. Full 3D simulations of elastic waves in real-world sized simulation spaces are extremely computationally demanding and require access to computational resources such as large computing clusters. We used Message Passing Interface (MPI) to create a customized parallel EFIT code that runs efficiently on a computing cluster at

NASA Langley. We used a 1D virtual topology for parallelization, breaking up the simulation space in the $\hat{x}_1$ direction. This partitioning means that all equations requiring stress or velocity values in the $+/-\hat{x}_1$ direction must have those values passed across processor boundaries, see figure 1.
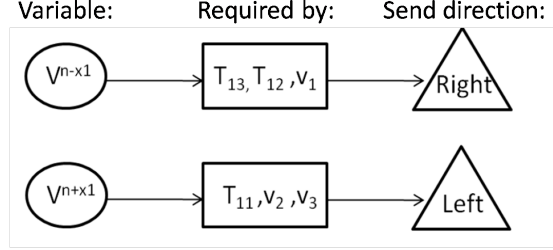

Figure 1: Diagram showing the variable passing required for EFIT with a 1D virtual topology.

Although EFIT equations can be found in the literature, below we give a brief mathematical description of the homogeneous EFIT equations for the reader's convenience. Inhomogeneous EFIT equations (which were used for the model verification in section 2.1) are available in several papers, such as [19], and will not be repeated here due to their additional length. Elastic wave propagation in isotropic media is described by Cauchy's equation for momentum and Hooke's Law. Taking the time derivative of these equations (in Cartesian coordinates) leads to nine equations for the velocities, v, and normal and shear stresses, T_{ij}. In FIT the equations are integrated over a control volume, and the integrals are approximated in a discrete form (details of this process can be found in [13]). To correctly transfer the equations into a discretized space, we place the stress and velocity components onto a discrete grid in the manner described by Fellinger [12]. For inhomogeneous material the Lamé parameters μ and λ, and the density, ρ, are also discretized leading to equations that can be found in the papers mentioned above. Below we list the nine discretized homogeneous EFIT equations describing wave propagation in isotropic material, where we assume $\Delta x_1 = \Delta x_2 = \Delta x_3$ [13]:

$$\dot{v}_1^{(n)}(t) = \frac{1}{\rho \Delta x}\left[T_{11}^{(n+\hat{x}_1)}(t) - T_{11}^{(n)}(t) + T_{12}^{(n)}(t) - T_{12}^{(n-\hat{x}_2)}(t) + T_{13}^{(n)}(t) - T_{13}^{(n-\hat{x}_3)}(t) \right] + f_1 \ ,$$

$$\dot{v}_2^{(n)}(t) = \frac{1}{\rho \Delta x}\left[T_{12}^{(n)}(t) - T_{12}^{(n-\hat{x}_1)}(t) + T_{22}^{(n+\hat{x}_2)}(t) - T_{22}^{(n)}(t) + T_{23}^{(n)}(t) - T_{23}^{(n-\hat{x}_3)}(t) \right] + f_2 \ ,$$

$$\dot{v}_3^{(n)}(t) = \frac{1}{\rho \Delta x}\left[T_{13}^{(n)}(t) - T_{13}^{(n-\hat{x}_1)}(t) + T_{23}^{(n)}(t) - T_{23}^{(n-\hat{x}_2)}(t) + T_{33}^{(n+\hat{x}_3)}(t) - T_{33}^{(n)}(t) \right] + f_3 \ ,$$

(1)

$$\dot{T}_{11}^{(n)}(t) = \frac{1}{\Delta x}\left[(\lambda^{(n)} + 2\mu^{(n)})(v_1^{(n)}(t) - v_1^{(n-\hat{x}_1)}(t)) + \lambda^{(n)}(v_2^{(n)}(t) - v_2^{(n-\hat{x}_2)}(t) + v_3^{(n)}(t)\right.$$
$$\left. -v_3^{(n-\hat{x}_3)}(t))\right] \quad ,$$

$$\dot{T}_{22}^{(n)}(t) = \frac{1}{\Delta x}\left[(\lambda^{(n)} + 2\mu^{(n)})(v_2^{(n)}(t) - v_2^{(n-\hat{x}_2)}(t)) + \lambda^{(n)}(v_1^{(n)}(t) - v_1^{(n-\hat{x}_1)}(t) + v_3^{(n)}(t)\right.$$
$$\left. -v_3^{(n-\hat{x}_3)}(t))\right] \quad , \tag{2}$$

$$\dot{T}_{33}^{(n)}(t) = \frac{1}{\Delta x}\left[(\lambda^{(n)} + 2\mu^{(n)})(v_3^{(n)}(t) - v_3^{(n-\hat{x}_3)}(t)) + \lambda^{(n)}(v_1^{(n)}(t) - v_1^{(n-\hat{x}_1)}(t) + v_2^{(n)}(t)\right.$$
$$\left. -v_2^{(n-\hat{x}_2)}(t))\right] \quad ,$$

$$\dot{T}_{12}^{(n)}(t) = \frac{\mu}{\Delta x}\left[(v_1^{(n+\hat{x}_2)} - v_1^{(n)}) + (v_2^{(n+\hat{x}_1)} - v_2^{(n)})\right] \quad ,$$
$$\dot{T}_{13}^{(n)}(t) = \frac{\mu}{\Delta x}\left[(v_1^{(n+\hat{x}_3)} - v_1^{(n)}) + (v_3^{(n+\hat{x}_1)} - v_3^{(n)})\right] \quad , \tag{3}$$
$$\dot{T}_{23}^{(n)}(t) = \frac{\mu}{\Delta x}\left[(v_2^{(n+\hat{x}_3)} - v_2^{(n)}) + (v_3^{(n+\hat{x}_2)} - v_3^{(n)})\right] \quad ,$$

where the notation $(n + \hat{x}_1)$ represents one spatial step in the $+\hat{x}_1$ direction beyond the current position, n, and the Lamé parameters relate to the longitudinal, c_L, and transverse, c_T, speeds of sound by $c_L = \sqrt{(\lambda + 2\mu)/\rho}$ and $c_T = \sqrt{\mu/\rho}$. The equations are discretized in time using central differences, which results in the velocity and stress components being staggered in time by $(\Delta t/2)$ [20]:

$$v_i^{(t)} = v_i^{(t-\Delta t)} + \dot{v}_i^{(t-\Delta t/2)}\Delta t \quad , \tag{4}$$

$$T_{ij}^{(t+\Delta t/2)} = T_{ij}^{(t-\Delta t/2)} + \dot{T}_{ij}^{(t)}\Delta t \quad , \tag{5}$$

where Δt and $\Delta t/2$ are full and half time steps. For each time step equations (1) - (3) are solved for all points in the simulation space. Using equations (1) through (5) the simulation proceeds forward in time.

Stability conditions require minimum time and spatial step sizes. We will use the same size spatial step in all directions since the discrete space is broken up into cubes. The reported ideal number of points per wavelength varies in the literature, ranging from $\lambda/8$ to $\lambda/15$ [21, 22]. The Courant-Friedrichs-Levy condition is used to determine the numerically stable time step size (with $\Delta x_1 = \Delta x_2 = \Delta x_3 = \Delta x$) [20, 22]:

$$\Delta t \approx \frac{\Delta x}{c_{max}\sqrt{3}} \quad , \quad \Delta x \approx \frac{c_{min}}{bf_{max}} \quad , \tag{6}$$

where c_{max} and c_{min} are the maximum and minimum wave speed, f_{max} is the maximum frequency, and b is a constant with the criteria that $b \geq 8$. For the case of an elastic solid in air, stress-free boundary conditions must be applied at the surfaces. Equations related to stress-free boundaries can be found in [20].

2.1   *Simulation Code Verification*

Implementation of the parallel 3D EFIT code was verified through various comparisons to analytical scattering solutions [23]. For example, we compared results from EFIT simulations of backscattering from an elastic sphere embedded in an elastic solid to a frequency domain analytical backscattering solution [24]. The EFIT time domain data was transformed into frequency domain for the comparison. Figure 2 shows the comparison for a broadband incident wave scattering from an aluminum sphere embedded in brass, where the spatial step size was $\lambda/20$. Note that since we did not include a perfectly matched layer at the simulation edges, the EFIT result differs slightly from the analytical result due to gating issues (i.e. edge reflections had to be gated out in time, thus also cutting out some of the backscattered waveform). We also point out that in order to minimize gating issues while maintaining a small step size, this comparison required a simulation space of 800 X 800 X 800 steps (512 million matrix elements for each time step, totaling around 0.8 TB of data) and took approximately 50 hours of runtime on 32 processors (1600 CPU hours).
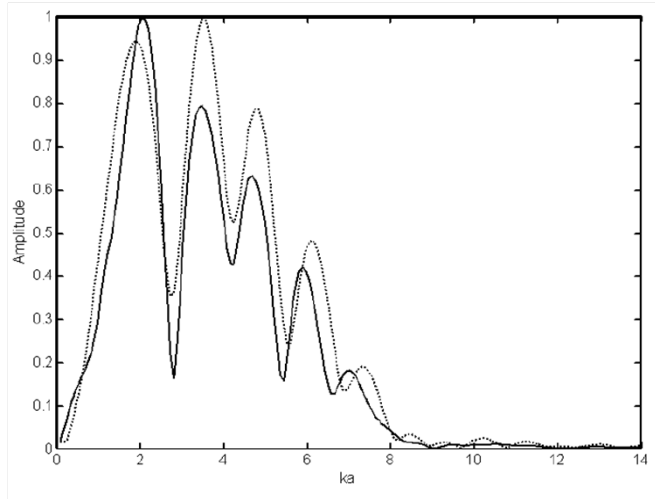

Figure 2: Comparison of frequency domain EFIT (dotted line) and analytical solution (solid line) backscattering results for an aluminum sphere embedded in brass, where ka is wavenumber multiplied by sphere radius.

3   Comparison to Experiment

We compared EFIT simulation and experimental results for Lamb wave interaction with a void-type flaw in an aircraft grade aluminum plate. These simulation results were compared to experimental data for code validation purposes and to explore the type of insight that the 3D simulations can provide in relation to experimental results. The experimental setup consisted of a rounded-rectangle flat-bottom hole milled into a 305 mm × 305 mm × 3.154 mm aluminum 2024 alloy plate with a rounded rectangle flaw of 76 mm in length and 30 mm in width. Experimental data was taken with a circular 6.35 mm (0.25 inch) diameter transducer with a center frequency of 2.15 MHz. The generated incident wave was a 5-cycle

sine wave tone burst. Glycerin was used as a couplant between a delay line and the plate surface. The transmitting and receiving transducers stepped through 100 locations spaced by 2 mm increments along both x and y axes of the plate, to cover a total scan area of 198 mm × 198 mm. This pitch-catch setup was used to collect the experimental data for all corresponding ray paths as the flaw was incrementally milled deeper. Data was taken at sixteen void depths (including 0 and 100% material loss).

For the corresponding EFIT simulations we incorporated the exact flaw shape and size. An incident wave of frequency 2.15 MHz and 5 cycles in length was introduced into the simulated plate. Each simulation took around 1400 CPU hours, and was completed in only 44 wall-clock hours with the parallelized code running on 32 processors. An example of EFIT simulation results is shown in figure 3. The images show the out-of-plane motion only (plotting in-plane motion would also be useful for visualizing certain modes). Another technique we used for the comparisons was to track Lamb mode conversion in the simulation output using a short time Fourier transform (STFT) in spatial domain. The technique creates plots of wavenumber versus position, and more details can be found in [23]. In this paper we will only give an overview of our results from numerous comparisons between experiment and simulation output.
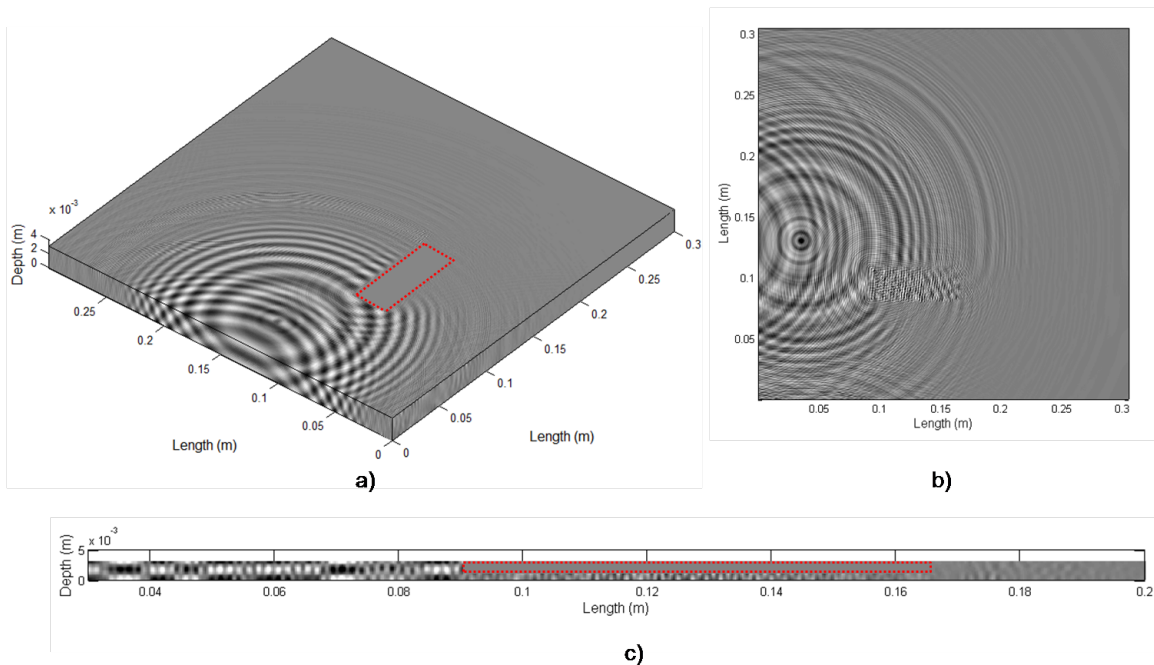

Figure 3: Example of EFIT simulation results (out-of-plane motion only) for a 3.154 mm thick aluminum plate with a 2.14 mm deep rounded rectangle flat bottom hole. The images show simulation output at a single point in time: a) 3D view showing the plate top and sides (flaw region outlined in red), b) 2D horizontal slice taken through the 3D space directly beneath the void showing waves propagating in the thinned region, c) 2D vertical slice showing the waves through the plate thickness (flaw region outlined in red).

The simulations showed that for some transducer positions and void depths certain Lamb wave modes were significantly disrupted due to interference effects created by waves interact-

ing with the flaw. In those cases the simulations helped explain the lack of detected modes in the experimental data. For other transducer locations we saw surprising results in the simulations which helped explain features in experimental data. Figure 4 shows simulation results, a spatial STFT plot, and experimental data for a case where the EFIT simulations predicted the creation of a high amplitude A0/S0 Lamb mode after the waves propagated beneath the void. Simulation images showed that this high amplitude mode was most likely due to constructive interference created by the exact shape and size of the flaw region. As shown in the figure, a high amplitude mode does indeed appear in the experimental data at the time expected from simulation results. Note that all locations of the Lamb mode labels in the figure showing experimental data were chosen based only on EFIT simulation results. The EFIT predicted mode arrival times for this example, and for many other cases we investigated, appear to match well with experimental data. Results for several comparisons between EFIT and experimental results can be found in [23]. The isotropic EFIT code will be used in the future to investigate other flaw types of interest. In the following section we briefly describe the extension of EFIT code to include anisotropic behavior for modeling wave behavior in composites.
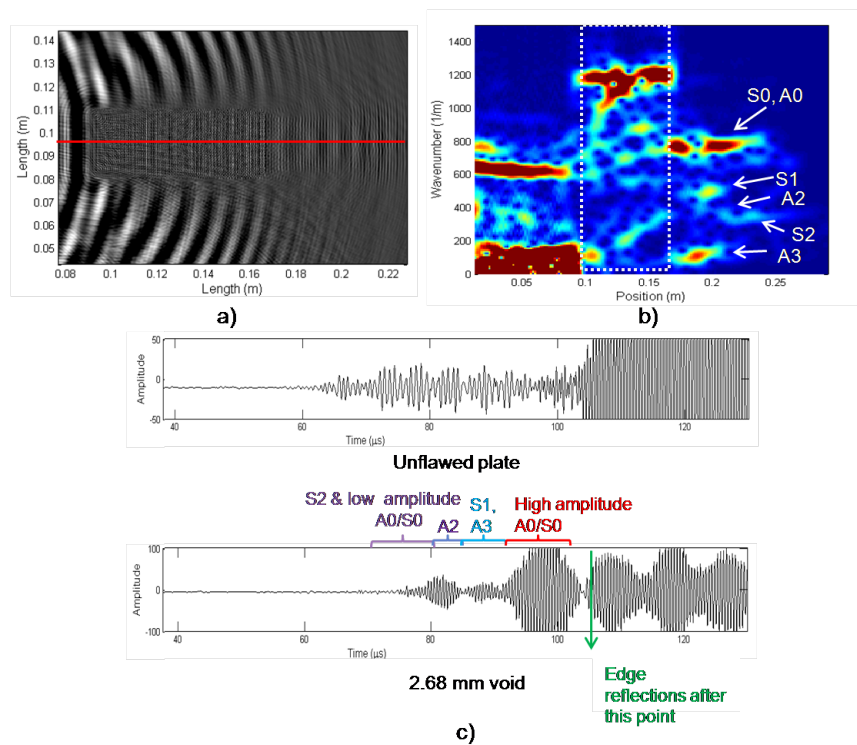

Figure 4: a) EFIT result showing a 2D slice beneath a 2.68 mm deep flat-bottom hole at a single point in time, b) Wavenumber versus position plot created from EFIT simulation data, corresponding to the A-scan position shown by red line in a) and to that same point in time. The region beneath the void falls within the white rectangle and Lamb wave modes emerging post-flaw are labeled, c) Denoised experimental data for the unflawed plate and the plate with a 2.68 mm deep flat-bottom hole. The Lamb wave mode label locations in c) were chosen based on the wavenumber versus position plots created using EFIT simulation data.

4   Anisotropic EFIT

As mentioned earlier, anisotropic versions of EFIT have been implemented previously by a few authors [16–18]. Most of the reported simulation results, however, were limited to 2D. Access to a large computing cluster will allow us to run 3D anisotropic elastic waves simulations. Incorporating anisotropy leads to significantly more complicated discretized stress equations compared to the homogeneous equations listed in section 2. The added complexity results from the fact that for a general triclinic anisotropic material the elastic matrix contains 21 different elastic constants [4]. To demonstrate this increase in complexity, below we list one of the 3D EFIT normal stress equations, T_{11}, for the case of anisotropic inhomogeneous material. Here we also point out that the ease of dealing with boundary conditions in EFIT makes it ideal for incorporating composite delaminations and other flaw types.

$$
\begin{aligned}
T_{11}^{(t+\Delta t/2)} &= T_{11}^{(t-\Delta t/2)} + \frac{\Delta t}{\Delta x} \left[c_{11}^{(n)}(v_1^{(n)} - v_1^{(n-\hat{x}_1)}) + c_{12}^{(n)}(v_2^{(n)} - v_2^{(n-\hat{x}_2)}) + c_{13}^{(n)}(v_3^{(n)} \right. \\
&\left. -v_3^{(n-\hat{x}_3)}) \right] + \frac{\Delta t}{4\Delta x} \left[c_{14}^{(n)} \left((v_2^{(n)} + v_2^{(n-\hat{x}_2)} + v_2^{(n+\hat{x}_3)} + v_2^{(n-\hat{x}_2+\hat{x}_3)}) - (v_2^{(n-\hat{x}_2)} + v_2^{(n)} \right. \right. \\
&+v_2^{(n-\hat{x}_2-\hat{x}_3)} + v_2^{(n-\hat{x}_3)}) + (v_3^{(n-\hat{x}_3)} + v_3^{(n)} + v_3^{(n+\hat{x}_2-\hat{x}_3)} + v_3^{(n+\hat{x}_2)}) - (v_3^{(n-\hat{x}_3)} + v_3^{(n)} \\
&+v_3^{(n-\hat{x}_2-\hat{x}_3)} + v_3^{(n-\hat{x}_2)})\Big) + c_{15}^{(n)} \left((v_1^{(n-\hat{x}_1)} + v_1^{(n)} + v_1^{(n-\hat{x}_1+\hat{x}_3)} v_1^{(n+\hat{x}_3)}) - (v_1^{(n-\hat{x}_1)} \right. \\
&+v_1^{(n)} + v_1^{(n-\hat{x}_1-\hat{x}_3)} + v_1^{(n-\hat{x}_3)}) + (v_3^{(n-\hat{x}_3)} + v_3^{(n)} + v_3^{(n+\hat{x}_1-\hat{x}_3)} + v_3^{(n+\hat{x}_1)}) - (v_3^{(n-\hat{x}_1-\hat{x}_3)} \\
&+v_3^{(n-\hat{x}_1)} + v_3^{(n-\hat{x}_3)} + v_3^{(n)})\Big) + c_{16}^{(n)} \left((v_1^{(n-\hat{x}_1)} + v_1^{(n-\hat{x}_1+\hat{x}_2)} + v_1^{(n)} + v_1^{(n+\hat{x}_2)}) \right. \\
&-(v_1^{(n-\hat{x}_1-\hat{x}_2)} + v_1^{(n-\hat{x}_1)} + v_1^{(n)} + v_1^{(n-\hat{x}_2)}) + (v_2^{(n-\hat{x}_2)} + v_2^{(n)} + v_2^{(n+\hat{x}_1-\hat{x}_2)} + v_2^{(n+\hat{x}_1)}) \\
&\left.\left. -(v_2^{(n-\hat{x}_1-\hat{x}_2)} + v_2^{(n-\hat{x}_1)} + v_2^{(n-\hat{x}_2)} + v_2^{(n)})\Big) \right]
\end{aligned}
\tag{7}
$$

5   Conclusion

We have developed a custom parallel 3D isotropic EFIT code to investigate Lamb wave scattering from damage in aerospace materials. We have found that 3D EFIT simulations can provide unique insight into complex Lamb wave behavior. The isotropic code implementation has been verified through comparisons with analytic solutions and has been compared against experimental results. In future work we plan to further develop and validate a 3D anisotropic EFIT code intended for modeling waves in composite materials. These computational tools will assist in the optimization of structural health monitoring flaw detection techniques for aerospace materials.

References

[1] K. Diamanti and C. Soutis. Structural health monitoring techniques for aircraft composite structures. Progress in Aerospace Sciences, 46:342–352, 2010.

[2] Kevin Leonard and Mark Hinders. Lamb wave tomography of pipe-like structures. Ultrasonics, 43:574–583, 2005.

[3] T Kundu, A Maji, T Ghosh, and K Maslov. Detection of kissing bonds by Lamb waves. Ultrasonics, 35:573–580, 1997.

[4] J.L. Rose. Ultrasonic Waves in Solid Media. Cambridge University Press, 1999.

[5] Victor Giurgiutiu and Adrian Cuc. Embedded non-destructive evaluation for structural health monitoring, damage detection, and failure prevention. Shock Vib Dig, 37(2):83–105, 2005.

[6] F Bellan, A Bulletti, L Capineri, L Masotti, G Yaralioglu, F Degertekin, B Khuri-Yakub, F Guast, and E Rosi. A new design and manufacturing process for embedded Lamb waves interdigital transducers based on piezopolymer film. Sensors and Actuators A, 123-124:379–387, 2005.

[7] Collet M, Ruzzene M, and Cunefare KA. Generation of Lamb waves through surface mounted macro-fiber composite transducers. Smart Materials and Structures, 20:1–14, 2011.

[8] Joseph L. Rose. A baseline and vision of ultrasonic guided wave inspection potential. J Press Vess Technol, 124:273–282, 2002.

[9] D Worlton. Ultrasonic testing with Lamb waves. Nondestructive testing, 158(4):218–222, 1957.

[10] J.P. Bingham and M.K. Hinders. Lamb wave pipe coating disbond detection using the dynamic wavelet fingerprinting technique. Rev Prog Quant Nondestr Eval, 29:615–622, 2010.

[11] T Weiland. A discretization method for the solution of maxwell's equations for six-component fields. Electron Commun (AEU), 31(3):116–120, 1977.

[12] F. Fellinger and K.J. Langenberg. Numerical techniques for elastic wave propagation and scattering. Proc IUTAM Symp, pages 81–86, July-Aug 1990.

[13] Rene Marklein. The finite integration technique as a general tool to compute acoustic, electromagnetic, elastodynamic, and coupled wave fields. In W.R. Stone, editor, Review of Radio Science: 1999-2002 URSI, pages 201–244. IEEE Press and John Wiley and Sons, New York, 2002.

[14] Frank Schubert, Bernd Koehler, and Pavel Zinin. Numerical time-domain simulation of wave propagation and scattering in acoustic microscopy for subsurface defect characterizaiton. Proc SPIE, 5766(106):106–117, 2005.

[15] Kevin Rudd, Kevin Leonard, Jill Bingham, and Mark Hinders. Simulation of guided waves in complex piping geometries using the elastodynamic finite integration technique. J Acoust Soc Am, 121(3):1449–1458, 2007.

[16] K. Nakahata, S. Hirose, F. Schubert, and B. Kohler. Image based EFIT simulation for nondestructive ultrasonic testing of austenitic steel. J Solid Mech Mater Eng, 3(12):1256–1262, 2009.

[17] S. Halkjaer. Elastic wave propagation in anisotropic, inhomogeneous materials: application to ultrasonic NDT. PhD thesis, Technical University of Denmark, 1999.

[18] J Hegemann, A Peiffer, B. Van Den Broucke, and H. Baier. Modeling of ultrasonic testing of woven fabric laminates: a microstructure approach. Rev Prog Quant Nondestr Eval, 28:1077–1082, 2009.

[19] P. Fellinger, R. Marklein, K.J. Langenberg, and S. Klaholz. Numerical modeling of elastic wave propagation and scattering with EFIT - elastodynamic finite integration technique. Wave Motion, 21:47–66, 1995.

[20] Jill Bingham and Mark Hinders. 3d elastodynamic finite integration technique simulation of guided waves in extended built-up structures containing flaws. J Comput Acoust, 18(2):1–28, 2010.

[21] F. Schubert, A. Peiffer, B. Kohler, and T. Sanderson. The elastodynamic finite integration technique for waves in cylindrical geometries. J Acoust Soc Am, 104:2604–2614, 1998.

[22] A. Peiffer and B. Kohler. The acoustic finite integration technique for waves of cylindrical symmetry (CAFIT). J Acoust Soc Am, 1997.

[23] C Leckey. Investigation of ultrasonic wave scattering effects using computational methods. Ph.D. Dissertation, College of William and Mary, 2011.

[24] M.K. Hinders. Plane-elastic wave scattering from an elastic sphere. Nuovo Cimento, 106B(7):799–818, 1991.